3844 *Macromolecules* **2010**, *43*, 3844–3850
DOI: 10.1021/ma100166a

Macromolecules
ARTICLE

Confinement Effects on Crystallization and Curie Transitions of Poly(vinylidene fluoride-*co*-trifluoroethylene)

Jodie L. Lutkenhaus,*,‡ Kathleen McEnnis,† Anatoli Serghei,† and Thomas P. Russell*,†

†*Department of Polymer Science and Engineering, Room A516, Conte Research Center, University of Massachusetts Amherst, 120 Governors Drive, Amherst, Massachusetts 01003, and* ‡*Department of Chemical Engineering, Room 300A, Mason Laboratory, Yale University, 9 Hillhouse Avenue, New Haven, Connecticut 06520*

Received January 21, 2010; Revised Manuscript Received March 9, 2010

ABSTRACT: Nanoscale patterning of piezoelectric and ferroelectric polymers, such as polyvinylidene fluoride (PVdF) and its copolymers with trifluoroethylene (PVdF-TrFE), is increasingly important in organic electronics, memory, and sensing. The nanoscale processing of polymers can lead to materials behavior that is strikingly different from the bulk because of confinement effects. Here we report the effects of confinement of PVdF-TrFE melt-wetted in porous templates of varying pore diameter. PVdF-TrFE is particularly interesting because it possesses a solid-state Curie transition, where both ferro and nonferroelectric phases crystallize into a paraelectric phase. Using modulated differential scanning calorimetry (MDSC), X-ray diffraction (XRD), and broadband dielectric spectroscopy (BDS), we demonstrate that confined PVdF-TrFE crystallizes into an oriented ferroelectric β phase. Both melting and crystallization temperatures decrease with decreasing pore diameter, and the Curie temperature is weakly affected. Results imply that nanoconfinement enhances the formation and orientation of the ferroelectric β phase and could potentially enhance ferroelectricty and piezoelectricity in nanoscale PVdF-TrFE features.

Introduction

Organic piezoelectric and ferroelectric materials, such as polyvinylidene fluoride (PVdF) and its copolymers with trifluoroethylene (PVdF-TrFE), generate electrical polarization in response to mechanical stimuli or electric fields (or vice versa).[1−8] Nanoscale patterning and processing of PVdF and PVdF-TrFE has elicited much interest in potential areas of organic electronics, sensors, energy storage, and nonvolatile memory.[9−16] However, nanoscale processing of polymers can lead to materials behavior that is strikingly different from that of the bulk.[17−20] At film thicknesses approaching the radius of gyration of the polymer, the polymer chain is perturbed and considered confined; subsequently, the polymer's phase behavior, orientation, and chain conformation are influenced. For example, polymers within confined geometries have demonstrated enhanced mobility, improved crystal orientation, homogeneous nucleation, and growth of crystals.[20−23]

Both PVdF and its copolymers have similar phase behavior. Homopolymer PVdF has multiple polymorphs of similar energy, of which the α phase and the β phase are the most common.[1] The most highly polar and most desired phase is the β phase, where chains of all-trans (*tttt*) conformation pack with dipoles parallel to a common axis in a pseudohexagonal configuration. The highly ordered and aligned dipoles in the β phase give rise to ferroelectric and piezoelectric behavior, piezoelectric constant of $d_{33,\mathrm{PVdF}} = -30$ pC/N[1] and $d_{33,\mathrm{PVdF\text{-}TrFE}} = -38$ pC/N.[24] However, homopolymer PVdF generally crystallizes into the nonpolar α phase, where chains of tg^+tg^- conformation pack with dipoles antiparallel. PVdF-TrFE readily crystallizes into the ferroelectric β phase because the addition of the third fluorine in the TrFE monomer unit sterically hinders the formation of the tg^+tg^- conformation.[3] At room temperature, PVdF-TrFE can exist as both ferroelectric and nonferroelectric crystalline phases. Above the Curie transition, PVdF-TrFE crystals are converted to a paraelectric phase via the introduction of $g^{\pm}$ bonds. The Curie transition typically appears as one or two overlapping first-order endothermic peaks upon heating (or exothermic peaks upon cooling) in differential scanning calorimetry.[3,4] The Curie transition of homopolymer PVdF is not observable and has been extrapolated to 205 °C, or 20° above its melting point.[4,25]

A broad understanding of the crystallinity, phase behavior, and orientation of PVdF-TrFE in confined dimensions is critically needed as the feature size of nanopatterned or templated PVdF-TrFE approaches dimensions near the radius of gyration of the polymer. Films of PVdF-TrFE as thin as 1 nm retained ferroelectric behavior and a distinct Curie transition,[10] which indicates that the polymer is capable of crystallizing into the β phase, even in extremely confined geometries. Interestingly, a second Curie-like transition, attributed to polymer−substrate interactions, was observed near room temperature in PVdF-TrFE films < 15 nm in thickness. Whereas Bune et al[10] observed two Curie transitions (one near bulk and one near room temperature), Jin et al.[26] observed a single Curie transition that dramatically decreased below a critical film thickness of 100 nm. The decreased Curie transition was ascribed to restricted crystal size and an increase in the number of defects. These conflicting reports highlight that phase transitions of PVdF-TrFe in thin films are not well understood.

The technique of melt-wetting cylindrical nanopores of controllable diameter with polymer provides a unique opportunity to study the phase behavior of confined PVdF-TrFE systematically.[15,27−29] Homopolymer PVdF melt-wetted into porous anodic aluminum oxide (AAO) templates demonstrated curvature-directed crystallization, where PVdF preferentially crystallized into the nonpolar α phase with crystal growth perpendicular

*Corresponding authors. E-mail: jodie.lutkenhaus@yale.edu; russell@mail.pse.umass.edu.

 Published on Web 03/25/2010

to the long axis of the pore.[21,22] In pores of diameter < 20 nm, homopolymer PVdF was highly constrained, and crystallization was inhibited.[30] Assuming that PVdF-TrFE behaves similar to homopolymer, confinement within cylindrical pores could potentially lead to highly oriented crystals.

Here we report the effects of confinement of PVdF-TrFE melt-wetted into porous AAO templates of varying pore diameter. Using modulated differential scanning calorimetry (MDSC), X-ray diffraction (XRD), and broadband dielectric spectroscopy (BDS), we demonstrate that confined PVdF-TrFE preferentially crystallizes into an oriented ferroelectric β phase. Both melting and crystallization temperatures decrease with decreasing pore diameter, and the Curie temperature is weakly affected. These results imply that nanoconfinement enhances the formation and orientation of the ferroelectric β phase and could potentially enhance ferroelectricty and piezoelectricity in nanoscale PVdF-TrFE features.

Experimental Section

General Sample Preparation. Poly(vinylidene fluoride-*co*-trifluoroethylene) (PVdF-TrFE) (M_n = 79 000 g/mol, PDI = 1.37) was dissolved in a 1:1 (v/v) mixture of dimethylformamide and acetone. The VdF/TrFE ratio was 70/30 and the supplier was Solvay. The 10 wt % solution was drop-cast onto a glass slide and dried overnight at 150 °C in a vacuum oven.

Anodized aluminum oxide (AAO) membranes were prepared from Al foil (99.99%, Sigma Aldrich) in a two-step anodization process.[31] The electrolyte solution used for anodization was either 0.3 M oxalic acid or 0.3 M sulfuric acid in deionized water. The first anodization time was 12 h, and the second anodization time was 24 h unless otherwise stated.

The AAO membrane was placed atop the dry, solution-cast PVdF-TrFE film and secured using clips. The AAO/PVdF-TrFE stack was placed in a 200 °C vacuum oven for 4 h, and then the temperature was lowered to 125 °C for 16 h. The stacks were allowed to cool to room temperature at less than 1 K/min.

Preparation of Scanning Electron Microscopy (SEM) Samples. The clips were removed, and the stack was placed in 5 wt % sodium hydroxide in deionized water to remove the back AAO surface. To remove the aluminum support, the stack was immersed in a copper(II) chloride solution with hydrochloric acid. The remaining stack was then immersed in sodium hydroxide solution, leaving behind nanotubes or nanorods supported by a bulk film. Samples were coated in 90 s of sputtered gold (~9 nm Au).

Preparation of Modulated Differential Scanning Calorimetry Samples. Following the removal of the back AAO surface, the sample was scraped away from the glass slide using a razor blade. The excess PVdF-TrFE surface film was dry-etched using a 47:3 O_2/CF_4 plasma in a Trion reactive ion etcher for 12 to 15 min. The template's surface was checked for complete removal of bulk using scanning force microscopy (Vecco Digital Instrument Dimension 3000). A piece of polyimide tape was placed against the etched surface to secure the sample. The aluminum support was removed using copper(II) chloride solution, leaving behind PVdF-TrFE-filled AAO membrane. For modulated DSC (TA Instruments Q200), the samples were heated to 170 °C, held isothermally for 5 min, cooled to 0 at 2 °C/min, held isothermally for 5 min, and heated to 170 at 2 °C/min. The amplitude was 1 °C, and the period was 50 s.

Preparation of X-Ray Diffraction Samples. The back AAO surface and excess PVdF-TrFE surface film were etched as before. The samples were studied using a PANalytical X'Pert X-ray diffractometer in reflective theta/two-theta mode. The sample was placed etched pore-side up so that the scattering vector was parallel to the pore axes. The scanning increment was 0.02°, and the integration time was 80 s.

Preparation of Samples for Broadband Dielectric Spectroscopy. After the second anodization process, the AAO membranes were detached from the aluminum substrates employing a third anodization procedure.[32] The AAO membranes were cleaned using oxygen plasma treatment for 20 min, followed by deposition of thin electrodes of gold on their both surfaces. Then, capillary filling of PVdF-TrFE into an AAO membrane was conducted at 170 °C under nitrogen. A full description of the cell and its design are described in ref 33 and elsewhere.[34] Then, the permittivity of the sample cell was measured at selected frequencies using a Solartron dielectric spectrometer assisted by a Quatro temperature controller. All dielectric experiments were carried out under nitrogen. The bulk layer was not removed from the interface with the AAO membrane during the dielectric investigations. However, the measurement cell was designed to measure the permittivity of the PVDF-TrFE confined within the nanopores alone by depositing the electrodes directly on both sides of the AAO membrane prior to infiltration.

Results and Discussion

PVdF-TrFE was melt-wetted into AAO templates of varying pore diameter at 200 °C. The entire pore length was wetted in < 4 h. Wetted templates were then annealed for 16 h at 125 °C, which is between the observed Curie point (T_c) and melting point (T_m), with the intention of promoting crystallization. Previous work indicates that annealing between the T_c and T_m leads to thick lamellar single crystals in the bulk.[35,36] Figure 1a shows nanotubes obtained from AAO membranes bearing pore diameters of 200 nm, and Figure 1b,c shows nanowires from AAO membranes bearing pore diameters of 40 and 15 nm, respectively. The nanotubes and wires appear flexible, and their dimensions are similar to the diameter and length of the template's pores.

The formation of PVdF-TrFE nanotubes in pores of 200 nm diameter and the formation of nanowires for pores of 40 and 15 nm diameter is consistent with the case of complete wetting. As described by Zhang et al.,[37] the spreading coefficient determines whether wetting is partial or complete. In the case of complete wetting, the spreading coefficient is positive, and a precursor film rapidly coats the inner wall of the cylindrical nanopore, coating all possible surfaces. If the diameter of the nanopore is larger than twice the thickness of the precursor film, then a nanotube is obtained; otherwise, a nanowire or rod results. The nanotube to nanowire transition observed from 200 to 40 nm pore diameter suggests that the thickness of the precursor film is somewhere between 100 and 20 nm. In the case of partial wetting, the spreading coefficient is negative, and the polymer melt fills the pore through capillary action, which yields nanowires or rods.

Because the process of complete wetting is rapid, the length of the nanotube or wire is challenging to control. We demonstrate control of nanowire length by careful variation of the template's pore length, which can be reproducibly tuned from the duration of the second anodization. Figure 2 shows SEM images of PVdF-TrFE nanorods and stubs obtained from alumina membranes bearing 40 nm diameter cylindrical pores of various anodization times (1 to 5 min). With increasing pore length (i.e., increasing anodization time), the aspect ratio of the nanowire increases from roughly 1 to 10. At a critical aspect ratio of about 4 to 6 (at 4 min anodization), the nanorods clump together. The observed clumping arises from the capillary forces during the rinsing and drying process, cohesion between neighboring nanostructures, and stiffness.

The thermal properties of PVdF-TrFE confined within cylindrical pores in alumina membranes were probed using MDSC. Conventional DSC merely probes total heat flow with changes in temperature, and separation of overlapping phenomena such as melting, crystallization, and Curie phase transitions is difficult. Modulated DSC, in which a sinusoidal temperature profile is superimposed onto a linear temperature sweep, is capable of separating phenomena occurring on time scales above and below

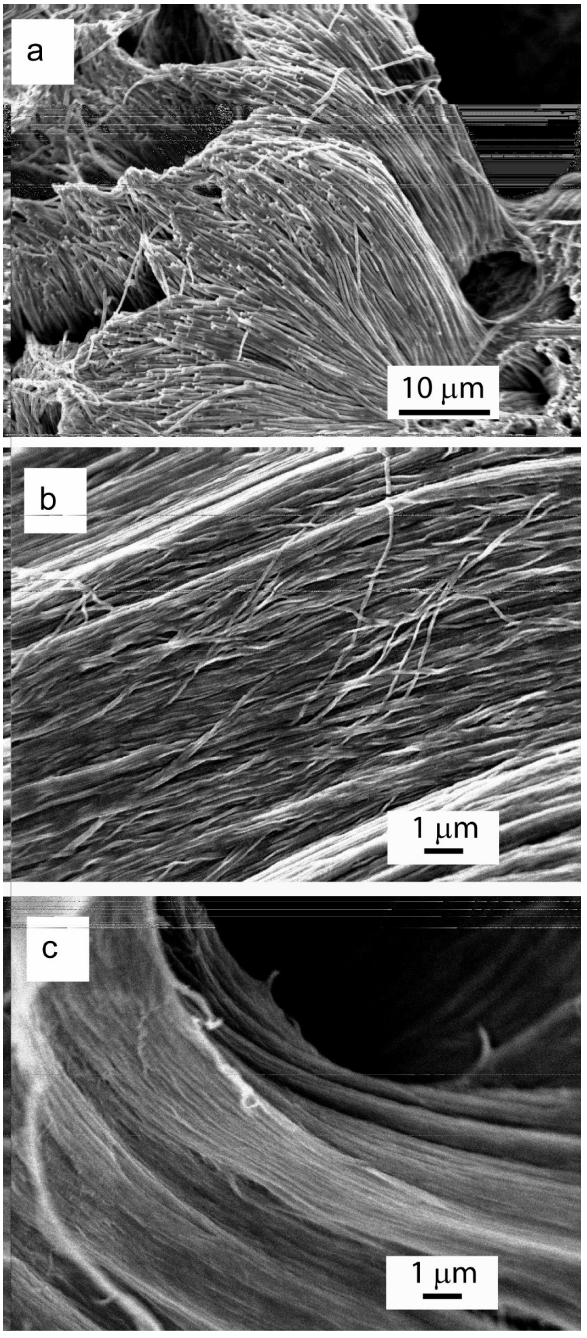

Figure 1. SEM images of templated PVdF-TrFE released from (a) 200, (b) 40, and (c) 15 nm AAO templates.

the period of the temperature modulation. This is especially valuable for cases where the heat flow signal is weak, as for our polymer-filled alumina templates. The "reversing" curve shows responses from phenomena occurring on time scales shorter than the modulation period (i.e., changes in heat capacity); the "nonreversing" curve captures phenomena occurring on time scales longer than the modulation period (i.e., kinetic events). The "total heat flow" curve is the arithmetic total of the reversing and nonreversing curve.

MDSC was performed on empty alumina membranes, bulk PVdF-TrFE, and alumina membranes melt-wetted with PVdF-TrFE. The polymer was melt-wetted into alumina membranes of 200, 40, and 15 nm diameter cylindrical pores. Bulk film on the membrane face was removed using O_2/CF_4 reactive ion etching. A thermogram of an empty AAO template was featureless (not shown). First, the total heat flow responses, which are analogous to conventional DSC, are discussed (Figure 3). Upon heating, bulk PVdF-TrFE underwent a Curie transition (117 °C) and bimodal melting (137 and 145 °C); upon cooling, the polymer crystallized (130 °C) and then had a Curie transition of two broad peaks (75 and 57 °C). The assignment of the respective events (Curie, crystallization, melting) was aided by BDS results, discussed later. Significant hysteresis of the Curie transition (~50°) was present upon heating and cooling. The PVdF-TrFE-filled alumina membrane with 200 nm diameter pores showed behavior similar to bulk polymer; although the magnitude of the 200 nm sample response was diminished, which we attribute to the presence of the alumina membrane. Nonetheless, the presence of the polymer within the template is clearly indicated by the features arising from MDSC.

The thermal responses of polymer-filled alumina membranes having 40 and 15 nm diameter cylindrical pores were distinctly different from those of bulk PVdF-TrFE and polymer-filled alumina membranes of 200 nm diameter (Figure 3). Upon heating, the total heat flow showed a single broad peak at 134 and 132 °C for the 40 and 15 nm polymer-filled alumina membranes, respectively. In contrast, bulk PVdF-TrFE and polymer-filled 200 nm AAO showed multiple first-order transitions. For the polymer within pores of 40 nm diameter or less, the melting temperature was depressed so that it coincided with the Curie transition. Upon cooling, a broad peak with weak maxima at 91 and 66 °C for 40 nm membranes and 91 and 69 °C for 15 nm membranes was observed. The sharp crystallization peaks observed for bulk and 200 nm membranes was not observed for the 40 and 15 nm membranes, which suggests that the broad exothermic peaks observed in cooling are overlapping crystallization and Curie transition events. In other words, crystallization from the melt is suppressed to lower temperatures in pores of 40 nm diameter or less. The overlapping Curie transition peaks appear to narrow and shift slightly to higher temperatures when pore diameter is <40 nm.

The observed influence of pore diameter on melting and crystallization signifies a transition from heterogeneous to homogeneous nucleation with decreasing pore diameter. As discussed by Steinhart[21,22] for the case of homopolymer PVdF in confinement, heterogeneous nucleation is typified by a sharp crystallization peak upon cooling in DSC, which we observe here for bulk and PVdF-TrFE confined in 200 nm diameter pores. A broad and supercooled crystallization transition, such as that for our samples of 40 and 15 nm pore diameter, is indicative of homogeneous nucleation where there are few defects to initiate crystal growth. When $d < 40$ nm, crystallization is depressed by >30 °C relative to bulk.

The Gibbs−Thompson equation[17,38,39] may be used to predict the melting point depression of a cylindrical nanocrystal of diameter, d, relative to T_m, its bulk melting temperature: $\Delta T_m = T_m - T_m(d) = 4\sigma_{sl}T_m/d\Delta H_f\rho_s$. Here σ_{sl} is the surface energy of the solid−liquid interface, ΔH_f is the bulk enthalpy of fusion, and ρ_s is the density of the solid. Because $\Delta T_m \approx 1/d$, we expect that ΔT_m ($d = 15$ nm) will be (8/3)*ΔT_m ($d = 40$ nm). Here ΔT_m ($d = 15$ nm) is 12.3 °C and ΔT_m ($d = 40$ nm) is 11.1 °C, which is a smaller deviation than the prediction of the Gibbs-Thompson equation. One reason for breakdown in the approximation is that the relation assumes that the enthalpy fusion is independent of confinement diameter. Previous work shows that such an assumption is not valid for all systems. Another reason for the failure of the G-T equation to describe the system accurately is that the smallest dimension investigated (15 nm) may be considered to be too large.

A close examination of the reversing and nonreversing curves indicates the relative time scales of the contributing Curie and melting/crystallization transitions (Figure 4). In all specimens examined, the magnitude of each transition in the nonreversing

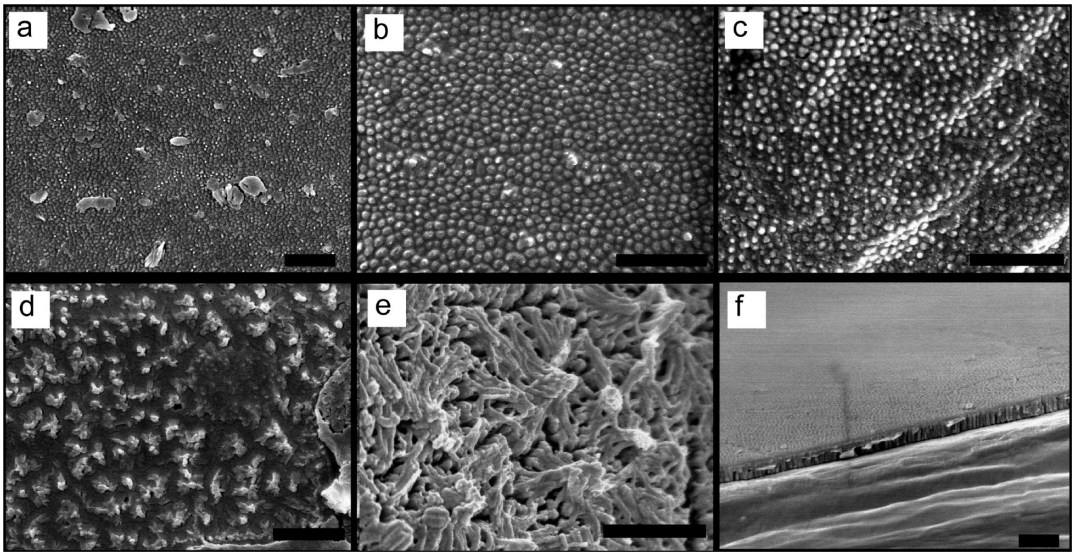

Figure 2. SEM images of templated PVdF-TrFE from AAO templates of 40 nm pore diameter and varying pore length. The second anodization time was varied (a) 1, (b) 2, (c) 3, (d) 4, and (e) 5 min. (f) Side view of an empty AAO template that had 2 min of second anodization. Scale bar is 1 μm.

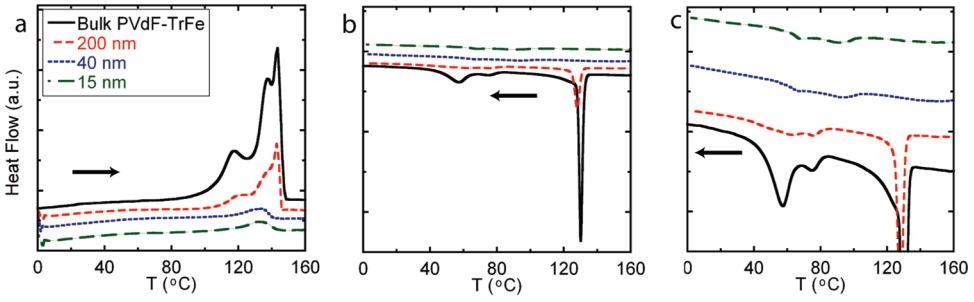

Figure 3. Total heat flow thermograms from modulated DSC of bulk PVdF-TrFE and PVdF-TrFE confined within AAO templates of 200, 40, and 15 nm diameter pores upon (a) heating and (b) cooling. (c) Epanded view of the cooling thermogram in part b. The solid black line represents bulk PVdF-TrFE; the long-dashed red line is polymer in 200 nm diameter pores, the short-dashed blue line is polymer in 40 nm diameter pores, and the long-dashed green line is polymer in 15 nm diameter pores. Curves are offset along the y axis for better clarity.

curve was larger than that of the reversing curve. This suggests that the time scales of melting, crystallization, and the para-to-ferroelectric Curie transition are longer than the period of modulation, 50 s. The observation of first-order transitions (Curie and melting) in the nonreversing curve is somewhat unusual because both are generally indicated by changes in heat capacity (captured by the reversing curve). However, this unusual behavior is possible for materials of high crystallinity. This longer time scale may also explain the apparent hysteresis of the Curie transition upon heating and cooling, where a large degree of supercooling is needed to initiate the para-to-ferroelectric phase transition. Thermal hysteresis arises from a change in available volume during the structural phase transition.[40] The modest response in the reversing curve is attributed to the rapid conversion of smaller, unstable crystals.

Of note, a weak and broad low-temperature peak (20−80 °C) was observed in the nonreversing heating curve for polymer confined within 15 nm pores. Similar results obtained via dielectric spectroscopy on planar PVdF-TrFE films show both a first-order low-temperature peak and high-temperature bulk Curie transition peaks for films < 15 nm in thickness.[10] The low-temperature peak was linked to surface layers of PVdF interacting with the supporting substrate. Here we attribute the low-temperature peak to the Curie transition of PVdF-TrFE surface layers on the aluminum oxide template wall. The observed high-temperature peak is attributed to "bulk" PVdF-TrFE within the pore.

Wide-angle XRD was performed on bulk PVdF-TrFE and PVdF-TrFE-filled AAO templates of 200, 40, and 15 nm pore diameter in reflection mode (Figure 5) such that the scattering vector is perpendicular to the template surface (i.e., parallel to the pore axis). Excess polymer on top of the AAO template was removed using reactive ion etching, and the template surface was checked using SFM. We assume that reflections of the polymer-filled AAO templates arise from PVdF-TrFE confined within the pores. XRD of an empty AAO template was featureless. Bulk PVdF-TrFE displayed peaks at 18.95 and 19.87 (200,110), 35.18 (001), and 40.88° (201,111). Results compare favorably to prior reports for bulk.[3,4] In general, the templated samples had lower intensity and a curve sloping downward, which we attribute to influence of the AAO template. Results similar to bulk were obtained for PVdF-TrFE within templates bearing 200 nm diameter pores. Polymer-filled templates of pore diameters 40 and 15 nm did not display c-axis relections (001, 201, 111), which indicates preferential crystal orientation of lamellae perpendicular to the pore axis.

Closer inspection of the (200,110) region (Figure 5b) indicated the presence of both nonferroelectric (18.93°) and ferroelectric (19.87°) phases in bulk PVdF-TrFE, where the intensity of the ferroelectric β-phase peak was roughly twice that of the nonferroelectric peak. Of note, the intensity of the nonferroelectric phase (200, 110) peak decreased relative to the β peak for the polymer-filled templates of 200, 40, and 15 nm pore diameter. Additionally, the (200,110) β-phase peak shifted slightly to larger scattering angles (or smaller d spacings) as pore diameter decreased. PVdF-TrFE within 40 and 15 nm diameter pores each had a β-phase peak at 20.21 and 20.10°, respectively. Rather than

crystallizing into a nonferroelectric phase, PVdF-TrFE may either solidify into an amorphous phase or crystallize into the β phase. Considering the weak intensity of the nonferroelectric phase, the remaining content within the nanocylindrical pores is likely composed of amorphous material. In confined geometries, crystallization to the β phase is likely preferred because the β phase is denser than the nonferroelectric, and chains are more efficiently packed in the β phase.[3]

A $T-d$ phase diagram was constructed from MDSC and room-temperature XRD experiments (Figure 6). The phase diagrams are divided into phases observed upon heating (Figure 6 a) or cooling (Figure 6 b) because of the significant hysteresis observed. At room-temperature bulk and confined PVdF-TrFE, both exist as mixed ferroelectric and nonferroelectric phases. Upon heating, bulk and PVdF-TrFE confined within 200 nm pores pass through a paraelectric phase before melting. With decreasing pore diameter, heating of the confined polymer results in melting directly from the ferroelectric and nonferroelectric phases. Cooling from the melt produces a similar phase diagram but with minor differences. For cooling, hysteresis shifts the phase transition regions to lower temperatures. Also, the paraelectric phase is present in a wider temperature range. In the phase transition region, multiple phases exist simultaneously.

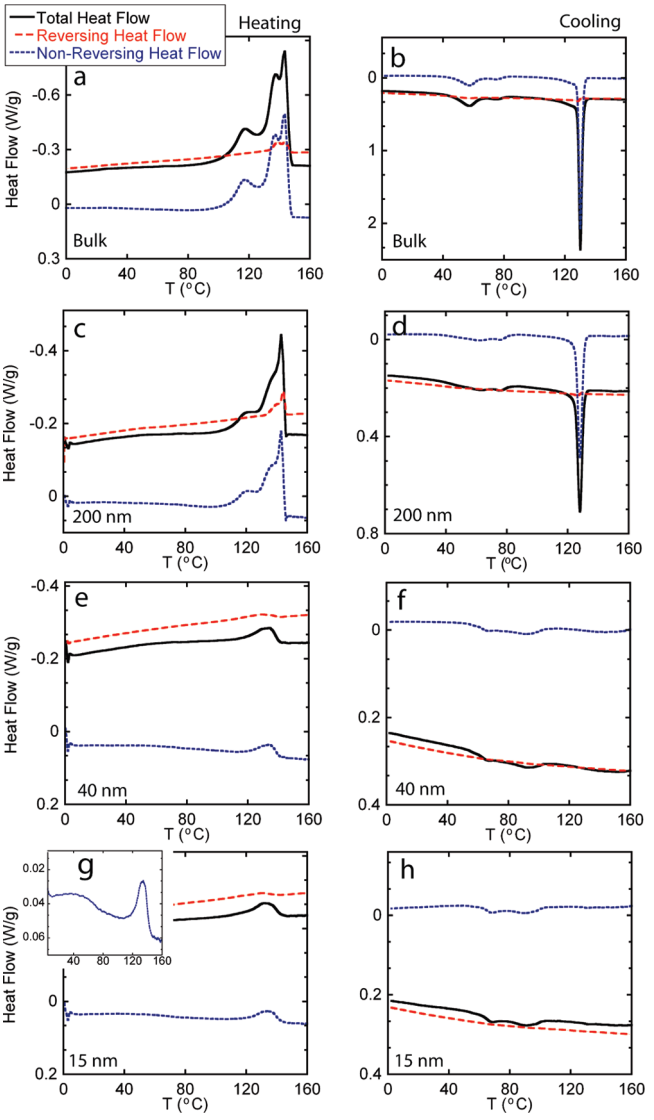

Figure 4. Modulated DSC thermograms of (a,b) bulk PVdF-TrFE and PVdF-TrFE confined within AAO templates of (c,d) 200, (e,f) 40, (g,h) and 15 nm diameter pores. (a,c,e,g) Heating curves. The inset in part g is an expanded view of the nonreversing curve. (b,d,f,,h) Cooling curves. The solid black line is the total heat flow, the long-dashed red line is the reversing heat flow, and the short-dashed blue line is the non-reversing heat flow.

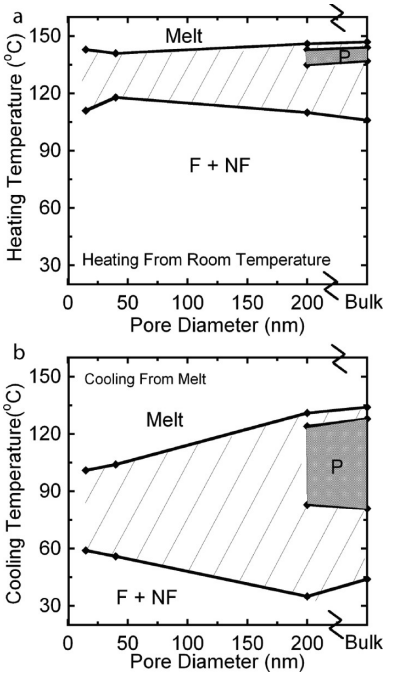

Figure 6. Phase behavior of PVdF-TrFE in cylindrical pores of varying diameter relative to bulk during (a) heating and (b) cooling. The black diamonds represent the lower and upper limits of peaks observed in MDSC. The dashed areas represent phase transition regions. Ferroelectric (F), nonferroelectric (NF), and paraelectric (P) phases are depicted. The gray region denotes the P phase.

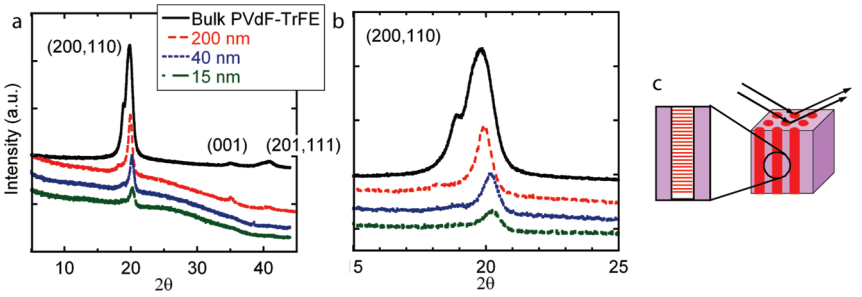

Figure 5. X-ray diffraction (a) of bulk PVdF-TrFE and PVdF-TrFE confined within AAO templates of 200, 40, and 15 nm diameter pores at room temperature. (b) Expanded view of the (200,110) region in part a. Curves are offset to enhance clarity. (c) Schematic of the XRD setup, where experiment was performed in theta-two theta mode. The scattering vector was perpendicular to the AAO template surface. An expanded, idealized view shows polymer crystals oriented relative to the pore axis.

It is possible that the paraelectric phase may coexist with other phases during the phase transition region when $d < 40$ nm.

BDS is a powerful experimental tool to investigate molecular fluctuations and charge transport processes in organic materials under a wide frequency and temperature range. A recent development shows that this experimental method can be also used to assess density fluctuations of polymer nano-objects.[33] At high frequencies in spectral regions not affected by dielectric dispersions, the permittivity function scales with the density, ρ, of the investigated material, as described by the Clausius−Mossotti equation

$$\frac{\varepsilon' - 1}{\varepsilon' + 2} = \frac{N_A \alpha_{mol}}{3\varepsilon_0 M}\rho \quad (1)$$

where N_A is the Avogadro constant, α_{mol} is the molecular polarizability, ε_0 is the vacuum permittivity, and M is the molecular mass. Derivation with respect to temperature leads to

$$\frac{\partial \varepsilon'}{\partial T}\left(\frac{3\varepsilon_0 M}{N_A \alpha_{mol}} - \rho\right) = \frac{\partial \rho}{\partial T}(\varepsilon' + 2) \quad (2)$$

which indicates a relation between the first derivative of permittivity and density

$$\frac{\partial \varepsilon'}{\partial T} \approx \frac{\partial \rho}{\partial T}$$

This proportionality relation is frequency-independent,[33] as expected in spectral regions where the contributions of relaxation processes and charge transport phenomena are negligible. Previous work indicates that the ferroelectric phase is denser than the paraelectric phase;[41] therefore, changes in density associated with melting, crystallization, and Curie transitions are expected to be apparent using BDS. PVdF-TrFE was filled into AAO membranes, and the permittivity at 100 kHz was measured upon cooling from melt at 1 °C/min and subsequent heating at the same rate (Figure 7).

BDS measurements upon cooling indicate crystallization and Curie transition processes. These phase transitions, accompanied by changes in density, can be analyzed by examining the first derivative of permittivity. Upon cooling of bulk PVdF-TrFE (Figure 7b), a sharp peak in the negative $d\varepsilon/dT$ quadrant at ~125 °C and two broad peaks in the positive $d\varepsilon/dT$ quadrant at ~80 and 50 °C are present. The negative peak is associated with a decrease in density, where PVdF-TrFE crystallizes into the paraelectric phase from the melt. The two positive peaks are associated with an increase in density from the Curie transition; previous work indicates that the ferroelectric phase is denser than the paraelectric phase.[41] Upon heating bulk PVdF-TrFE (Figure 7a), BDS measurements indicate a Curie transition at ~115 °C and a bimodal melting process at ~137 and 143 °C, accompanied by the corresponding changes in density. In this manner, BDS measurements (which describe changes in density) can complement MDSC measurements (which describe changes in heat capacity).

Similar measurements were performed for PVdF-TrFE confined within AAO membranes (Figures 7c−h) and are described in detail in ref 33. Upon cooling of the confined polymer, Curie transitions are indicated, and their temperature is similar to that of bulk polymer. Also, upon cooling, PVdF-TrFE confined within 40 and 15 nm pores shows crystallization at bulk and suppressed temperatures overlapping with the bimodal Curie transition. These results contrast data from MDSC, where calorimetric measurements indicate no bulk-like crystallization events for PVdF-TrFE within 40 and 15 nm pores. A possible reason is that MDSC and BDS measurements were performed under different heating and cooling rates. We also speculate that BDS gives sensitive access to density fluctuations that are not observable using calorimetric methods. A more thorough investigation is planned using other polymeric materials.

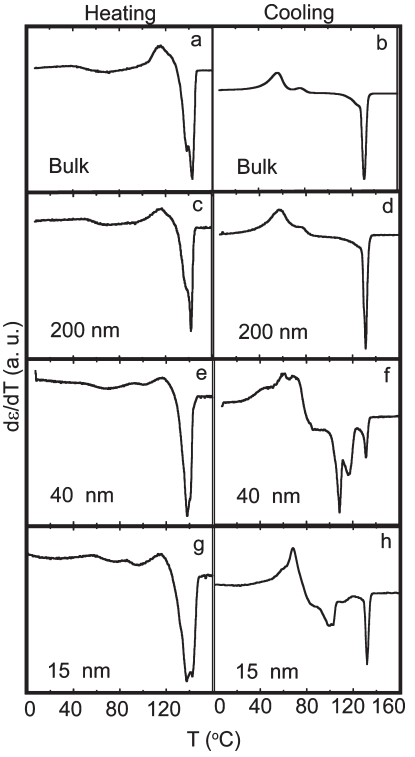

Figure 7. First derivative of ε' measured upon heating (left column) and cooling (right column) at 1 °C/min for (a,b) PVDF-TrFE in the bulk and PVdF-TrFE confined within AAO templates of (c,d) 200, (e,f) 40, and (g,h) 15 nm diameter pores. (a,c,e,g) Heating curves. (b,d,f,h) Cooling curves. Adapted from ref 33.

For heating of PVdF-TrFE confined within AAO membranes, BDS results mirror those from MDSC. For pore diameters as small as 15 nm, a Curie transition at 112 °C and a bimodal melting process are observed. Also, a broad and weak Curie transition was observed for PVdF-TrFE in 15 nm diameter pores, which is also observed in MDSC. This indicates that the ferroelectric phase is preserved down to pore sizes as small as 15 nm.

Conclusions

The influence of confinement on the phase behavior, crystallization, and orientation of PVDF-TrFE within cylindrical nanopores was investigated. Significant deviation from bulk behavior was observed for PVdF-TrFE within pores of <40 nm diameter. Crystallization of the polymer into the β-phase was enhanced, and the nonferroelectric phase was suppressed. The crystal lamellae were oriented perpendicular to the pore axis. Both melting and crystallization were depressed, indicating unstable crystals and homogeneous nucleation. The Curie transition was only slightly affected. Upon heating, the Curie transition coincided with melting; upon cooling, the Curie transition region narrowed. A second broad Curie transition near room temperature was observed for PVdF-TrFE confined within 15 nm pores, similar to results of thin films.[10] Results suggest that confinement could potentially enhance the ferroelectric and piezoelectric response of PVdF-TrFE via oriented crystallization of ferroelectric domains.

Acknowledgment. J. L. Lutkenhaus thanks Yale University for postdoctoral support. This work was supported by Yale University (J.L.L.), the U.S. Department of Energy (DOE) under

contract no. DE-FG-0296ER45612 (T.P.R.; A.S.), and DE-FG-0296ER42126 (T.P.R.). We also thank Dr. Charles Potter of TA Instruments for insightful discussion of thermal analysis data.

References and Notes

(1) Lovinger, A. J. *Science* **1983**, *220*, 1115–1121.
(2) Kawai, H. *Jpn. J. Appl. Phys.* **1969**, *8*, 975.
(3) Calleja, F. J. B.; Arche, A. G.; Ezquerra, T. A.; Cruz, C. S.; Batallan, F.; Frick, B.; Cabarcos, E. L. *Adv. Polym. Sci.* **1993**, *108*, 1–48.
(4) Koga, K.; Ohigashi, H. *J. Appl. Phys.* **1986**, *59*, 2142–2150.
(5) Kepler, R. G.; Anderson, R. A. *J. Appl. Phys.* **1978**, *49*, 1232–1235.
(6) Kepler, R. G.; Anderson, R. A. *J. Appl. Phys.* **1978**, *49*, 4490–4494.
(7) Furukawa, T. *Phase Transitions* **1989**, *18*, 143–211.
(8) Zhang, Q. M.; Bharti, V.; Zhao, X. *Science* **1998**, *280*, 2101–2104.
(9) Hu, Z. J.; Tian, M. W.; Nysten, B.; Jonas, A. M. *Nat. Mater.* **2009**, *8*, 62–67.
(10) Bune, A. V.; Fridkin, V. M.; Ducharme, S.; Blinov, L. M.; Palto, S. P.; Sorokin, A. V.; Yudin, S. G.; Zlatkin, A. *Nature* **1998**, *391*, 874–877.
(11) Rankin, C.; Chou, C. H.; Conklin, D.; Bonnell, D. A. *ACS Nano* **2007**, *1*, 234–238.
(12) Zhang, L.; Ducharme, S.; Li, J. *Appl. Phys. Lett.* **2007**, *91*, 3.
(13) Kang, S. J.; Park, Y. J.; Hwang, J.; Jeong, H. J.; Lee, J. S.; Kim, K. J.; Kim, H. C.; Huh, J.; Park, C. *Adv. Mater.* **2007**, *19*, 581.
(14) Asadi, K.; De Leeuw, D. M.; De Boer, B.; Blom, P. W. M. *Nat. Mater.* **2008**, *7*, 547–550.
(15) Cepak, V. M.; Martin, C. R. *Chem. Mater.* **1999**, *11*, 1363–1367.
(16) Hu, Z.; Baralia, G.; Bayot, V.; Gohy, J. F.; Jonas, A. M. *Nano Lett.* **2005**, *5*, 1738–1743.
(17) Alcoutlabi, M.; McKenna, G. B. *J. Phys.: Condens. Matter* **2005**, *17*, R461–R524.
(18) Russell, T. P. *Curr. Opin. Colloid Interface Sci.* **1996**, *1*, 107–115.
(19) Priestley, R. D.; Ellison, C. J.; Broadbelt, L. J.; Torkelson, J. M. *Science* **2005**, *309*, 456–459.
(20) Loo, Y. L.; Register, R. A.; Ryan, A. J.; Dee, G. T. *Macromolecules* **2001**, *34*, 8968–8977.
(21) Steinhart, M.; Senz, S.; Wehrspohn, R. B.; Gosele, U.; Wendorff, J. H. *Macromolecules* **2003**, *36*, 3646–3651.
(22) Steinhart, M.; Goring, P.; Dernaika, H.; Prabhukaran, M.; Gosele, U. *Phys. Rev. Lett.* **2006**, *97*, 027801.
(23) Shin, K.; Obukhov, S.; Chen, J. T.; Huh, J.; Hwang, Y.; Mok, S.; Dobriyal, P.; Thiyagarajan, P.; Russell, T. P. *Nat. Mater.* **2007**, *6*, 961–965.
(24) Omote, K.; Ohigashi, H.; Koga, K. *J. Appl. Phys.* **1997**, *81*, 2760–2769.
(25) Lovinger, A. J.; Davis, D. D.; Cais, R. E.; Kometani, J. M. *Macromolecules* **1986**, *19*, 1491–1494.
(26) Jin, X. Y.; Kim, K. J.; Lee, H. S. *Polymer* **2005**, *46*, 12410–12415.
(27) Steinhart, M.; Wendorff, J. H.; Greiner, A.; Wehrspohn, R. B.; Nielsch, K.; Schilling, J.; Choi, J.; Gosele, U. *Science* **2002**, *296*, 1997.
(28) Zheng, R. K.; Chan, H. L. W.; Choy, C. L. *Nanotechnology* **2005**, *16*, 1928–1934.
(29) Zheng, R. K.; Yang, Y.; Wang, Y.; Wang, J.; Chan, H. L. W.; Choy, C. L.; Jin, C. G.; Li, X. G. *Chem. Commun.* **2005**, *11*, 1447–1449.
(30) Martin, J.; Mijangos, C.; Sanz, A.; Ezquerra, T. A.; Nogales, A. *Macromolecules* **2009**, *42*, 5395–5401.
(31) Masuda, H.; Fukuda, K. *Science* **1995**, *268*, 1466–1468.
(32) Zhao, S.; Roberge, H.; Yelon, A.; Veres, T. *J. Am. Chem. Soc.* **2006**, *128*, 12352–12353.
(33) Serghei, A.; Miranda, D.; McEnnis, K.; Lutkenhaus, J.; Kremer, F.; Russell, T. P., submitted to *Nano Letters*.
(34) Serghei, A.; Chen, D.; Lee, D. H.; Russell, T. P. *Soft Matter* **2010**, *6*, 1111.
(35) Ohigashi, H.; Akama, S.; Koga, K. *Jpn. J. Appl. Phys., Part 1* **1988**, *27*, 2144–2150.
(36) Cabarcos, E. L.; de las Rivas, B.; Ezquerra, T. A.; Calleja, F. J. B. *Macromolecules* **1998**, *31*, 6157–6163.
(37) Zhang, M. F.; Dobriyal, P.; Chen, J. T.; Russell, T. P.; Olmo, J.; Merry, A. *Nano Lett.* **2006**, *6*, 1075–1079.
(38) Bassett, D. C.; Davitt, R. *Polymer* **1974**, *15*, 721–728.
(39) Gibbs, J. W. *The Collected Works of J. Willard Gibbs*; Longmans, Green and Co.: New York, 1928.
(40) Cabarcos, E. L.; Braña, A. F.; Frick, B.; Batallan, F. *Phys. Rev. B* **2007**, *76*, 064308.
(41) Lando, J. B.; Doll, W. W. *J. Macromol. Sci., Part B: Phys.* **1968**, *2*, 205–218.